EES Catalysis

PAPER

View Article Online
View Journal | View Issue

Open Access Article. Published on 22 April 2025. Downloaded on 3/15/2026 10:17:58 AM.
This article is licensed under a Creative Commons Attribution-NonCommercial 3.0 Unported Licence.

Check for updates

Cite this: *EES Catal.*, 2025, 3, 811

Visible-light photocatalytic CO_2 hydrogenation using surface-alloyed plasmonic AgPt nanoprisms†

Garv Bhardwaj,[a] Fergus McLaren,[b] Kishan S. Menghrajani,[c] Sanje Mahasivam,[b] Stefan A. Maier,[cd] Murali Sastry[ab] and Akshat Tanksale *[a]

Received 16th February 2025,
Accepted 16th April 2025

DOI: 10.1039/d5ey00046g

rsc.li/eescatalysis

Development of suitable catalysts for light-driven CO_2 hydrogenation is an alluring goal in catalysis. In this study, plasmonic Ag nanoprisms were combined with Pt to make surface-alloyed nanoparticles for aqueous-phase CO_2 hydrogenation. The Pt loading favoured the product selectivity towards multi-electron C_1 products and promoted acetic acid production *via* C–C coupling. Increasing the reaction pressure further improved acetic acid production where the highest yield of 0.491 mmol g_{cat}^{-1} was achieved at 20 bar. Within the visible-light region, the in-plane dipole resonance peak of $Ag_{91}Pt_9$ at 600 nm contributed the highest apparent quantum yield of 26.7%. These investigations demonstrated the significance of designer plasmonic catalysts and highlighted their photocatalytic enhancement towards CO_2 conversion.

Broader context

Photocatalytic CO_2 conversion to valuable C_1–C_2 chemicals offers a low carbon intensity pathway to combat climate change and replace fossil fuels as feedstock. This study focuses on enhancing photocatalytic activity by developing plasmonic surface-alloyed AgPt nanoprisms, to convert CO_2 in an aqueous environment at room temperature. The addition of Pt enhances productivity towards a variety of chemicals, particularly acetic acid. The investigations on using visible-light illumination and achieving high apparent quantum yield underscore the ability of plasmon-mediated photocatalysis to enhance CO_2 conversion. These findings highlight the potential of using plasmonic materials as photocatalysts.

Introduction

Carbon capture, utilisation and storage (CCUS) technologies have expanded over the last decade, supporting the emissions reduction target towards creating a circular economy.[1] Bulk chemical production from CO_2 offers an opportunity to displace conventionally used fossil-derived chemicals. Carbon-neutral chemicals can be produced by hydrogenating the captured CO_2 using green hydrogen.[2] Photocatalytic CO_2 hydrogenation is an emerging area of interest due to its potential to utilise sunlight.[3]

Semiconductor photocatalysts have been studied extensively for CO_2 hydrogenation to produce C_1 chemicals such as carbon monoxide (CO),[4,5] methane (CH_4),[4–7] formic acid (HCOOH),[8–10] formaldehyde (HCHO)[11,12] and methanol (CH_3OH)[13–15] and C_2 chemicals including acetic acid (CH_3COOH),[8] acetaldehyde (CH_3CHO),[16] ethane (C_2H_6)[5,12] and ethanol (C_2H_5OH).[16,17] The major challenges of photocatalytic CO_2 reduction and hydrogenation can be attributed to (1) poor multi-component catalyst design hindering light-to-energy transfer, (2) limited light absorption range, and (3) limited control of product selectivity because of a lack of understanding of reaction pathway. Plasmonic nanomaterials have garnered interest for various applications,[18–20] including their potential as photocatalysts.[21–24] Noble metal nanoparticles (NPs) made of silver (Ag), gold (Au) and copper (Cu) can capture the incident light through the collective excitation of conduction electrons. The spatial confinement of this excitation because of a NP's exterior boundary results in a resonant oscillation, known as the localised surface plasmon resonance (LSPR).[25,26] LSPR produces a local electric field amplification and decay by creating hot charge carriers and phonon vibrations.[27,28]

Ag provides several advantages over other plasmonic metals (*e.g.* Au, Cu) including high plasmon quality factor, tunable

[a] Department of Chemical and Biological Engineering, Monash University, VIC 3800, Australia. E-mail: Akshat.Tanksale@monash.edu
[b] Department of Material Science and Engineering, Monash University, VIC 3800, Australia
[c] School of Physics and Astronomy, Monash University, VIC 3800, Australia
[d] Department of Physics, Imperial College London, London SW7 2AZ, UK

† Electronic supplementary information (ESI) available. See DOI: https://doi.org/10.1039/d5ey00046g

© 2025 The Author(s). Published by the Royal Society of Chemistry

Open Access Article. Published on 22 April 2025. Downloaded on 3/15/2026 10:17:58 AM.
This article is licensed under a Creative Commons Attribution-NonCommercial 3.0 Unported Licence.

optical properties and distinguishable interband and intraband transitions.[29] Various factors affect LSPR such as particle size, morphology, composition and surrounding environment.[30] Among these, silver nanoprism-like morphology has multiple tunable LSPR modes in the visible region and higher photocatalytic performance.[31,32] Ag-based catalysts have shown CO_2 activation. However, co-catalysts are required to enhance the photocatalytic properties. Combining Ag with a catalytically active metal such as platinum (Pt) can overcome the challenges with photocatalysts in hydrogenating CO_2.[33–37] Researchers have also found the plasmon energy transfer within Ag–Pt nanocubes useful for photochemical reactions.[38,39]

Here, we show plasmon-mediated photocatalytic capability of surface-alloyed AgPt nanoprisms (NPrs) in and aqueous-phase CO_2 hydrogenation reaction to produce HCOOH, HCHO and CH_3COOH. The AgPt NPrs were synthesised through galvanic replacement reaction (GRR) of Pt with Ag NPrs. The deposition of Pt on the Ag NPrs was surface-limited, which formed Ag–Pt alloys. The catalyst performance improved significantly with increasing Pt loading and reaction pressure. Control experiments confirmed the visible-light-driven photocatalysis consuming CO_2 and H_2. The in-plane dipole resonance peak was majorly responsible for the catalytic performance. We also investigated catalyst deactivation through colloidal instability. The reaction pathway was interpreted based on the catalyst selectivity and hydrogenation of selected intermediates.

Results

Materials characterisation

Ag nanoprisms (Ag NPrs) were synthesised according to the method developed by Aherne and co-authors with modifications to increase sample concentration.[40] The colloidal synthesis produced a high proportion of platelet nanoprisms (NPr) (77%), which were categorised into triangles (29%) with an edge length of 63 ± 10 nm, and discs (48%) with a diameter of 42 ± 6 nm (Fig. S.1, S.2 and Table S.1, ESI†). Pt was incorporated in the Ag NPr by a galvanic replacement reaction (GRR) using K_2PtCl_4. The Pt loadings were calculated from the total moles of Ag and Pt used in synthesis, and samples were labelled $Ag_{100-x}Pt_x$, where x corresponded with loadings from 1.5–9 mol% Pt, assuming complete GRR. The UV-vis spectra of Ag NPrs and AgPt NPrs showed both red-shift and dampening of the in-plane dipole resonance peak of Ag NPr at 600 nm, proportional to the Pt loadings (Fig. 1 and Table S.2, ESI†). This was attributed to the galvanic etching of Ag NPr and Ag–Pt alloy formation on the NPr surface.[41–45] In comparison, the Pt NP spectra did not show any appreciable plasmon resonance peaks in the wavelength region (Fig. 1).

In comparison with as-synthesised Ag NPrs (Fig. 2A), edge deformation was observed in bright field scanning transmission electron microscopy (BF-STEM) micrographs for all AgPt NPrs with varying Pt loadings (Fig. 2C, E, G and I). Between samples, the dimensions of the NPrs (Fig. S.2C, ESI†) and the degree of edge deformation did not vary significantly, but

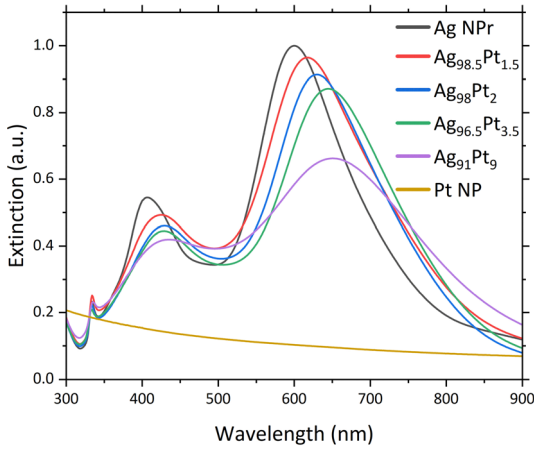

Fig. 1 UV-vis spectra of AgPt surface alloyed catalyst with different Pt loading.

Kirkendall voids were present in at higher Pt loadings (Fig. 2I and J) which may contribute to the non-linear relationship between Pt concentration and in-plane dipole resonance wavelength (Table S.2, ESI†).

STEM energy dispersive spectroscopy (STEM-EDS) mapping of clusters of NPrs was used to quantify Ag/Pt composition of the samples (Table 1) and confirmed that free Pt NPs were not present. Mapping of individual NPrs at all loadings revealed Pt was distributed across the entire surface but was concentrated at the edges of the triangular face (Fig. 2C–J). As STEM-EDS is a depth-insensitive technique, EDS line scans of $Ag_{91}Pt_9$ at different orientations were collected (Fig. S.3, ESI†). Pt was most abundant at the edges of the NPrs in both orientations, and a pronounced minimum of Pt occurred at the centre of the NPr in the edge-on case. Given these results and previous literature showing the surface-limited nature of alloy formation through galvanic processes, the Pt deposition was determined to be surface-limited.[42,46]

The crystal structure of the NPrs was studied using selected area electron diffraction (SAED) (Fig. 2M). In agreement with Aherne and co-authors, peaks for HCP {1010}, FCC {111} and {220} planes were identified in the Ag NPr sample.[40] Based on Vegard's Law and the lattice parameters of Ag (4.08 Å) and Pt (3.92 Å), a linear expansion of the real space inter-planar distances with increasing Pt concentration was expected. As Pt concentration increased up to $Ag_{96.5}Pt_{3.5}$, the HCP {1010} and FCC {111} peak positions remained unchanged, while the FCC {220} peak underwent a small reciprocal space expansion consistent with Ag–Pt alloying under Vegard's Law. HCP {1010} and FCC {111} planes occurred on the flat triangular faces and through the interior of the NPr, while FCC {220} planes were predominantly present at the edges and tips. The change to only the {220} peak position suggests that, at concentrations at or below 3.5%, Pt was mainly deposited along the NPr edges.

However, at $Ag_{91}Pt_9$, the crystallography of the sample changed considerably. The HCP {1010} peak was still present, though shifted from 4.06 nm^{-1} in Ag to 3.99 nm^{-1} in $Ag_{91}Pt_9$. Similarly, the FCC {220} peak shifted from 7.03 nm^{-1} in Ag to 6.87 nm^{-1} in $Ag_{91}Pt_9$ in a reversal of trend observed at lower Pt

 © 2025 The Author(s). Published by the Royal Society of Chemistry

Open Access Article. Published on 22 April 2025. Downloaded on 3/15/2026 10:17:58 AM.
This article is licensed under a Creative Commons Attribution-NonCommercial 3.0 Unported Licence.

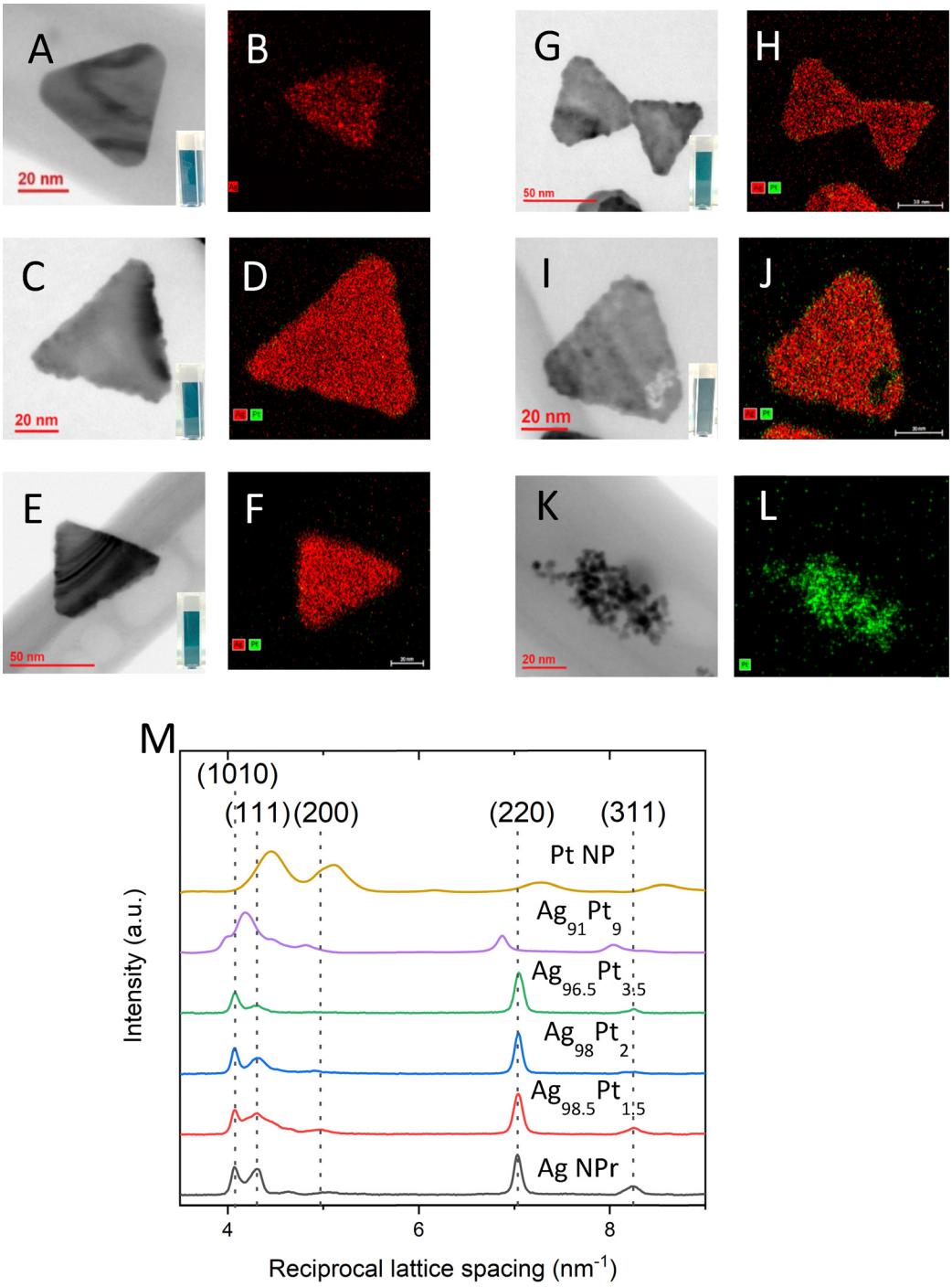

Fig. 2 (A)–(L) STEM-EDS micrographs of (A) and (B) Ag NPr (C) and (D) $Ag_{98.5}Pt_{1.5}$ (E) and (F) $Ag_{98}Pt_2$ (G) and (H) $Ag_{96.5}Pt_{3.5}$ (I) and (J) $Ag_{91}Pt_9$ (K) and (L) Pt NP (inset of STEM micrographs shows corresponding bulk sample solutions) with corresponding elemental maps of Ag (red) and Pt (green) (M) rotational averages of selected area diffraction (SAED) patterns of corresponding catalysts.

concentrations (where the peak gradually shifted from 7.03 nm^{-1} to 7.05 nm^{-1}). The large peak at 4.18 nm^{-1} did not align with any of the expected reflections. Based on the lattice parameter of Ag, the FCC {111} reflection can be calculated to be 4.23 nm^{-1}, but in the Ag NPr sample, FCC {111} was observed at 4.30 nm^{-1}. It was unlikely that the 4.18 nm^{-1} peak is FCC {111}, as this would require a significant shift from the corresponding Ag NPr peak in the opposite direction to what was expected from AgPt alloying. However, given similar shifts occurred for the HCP {1010} and FCC {220} peaks in this sample, the FCC {111} assignment cannot be ruled out. The other explanation for the 4.18 nm^{-1} peak is an Ag–Pt alloy phase of HCP {1010}. Pt has been observed to adopt an HCP lattice structure when deposited on another HCP surface and may be responsible for the anomalous peak.[47,48]

Open Access Article. Published on 22 April 2025. Downloaded on 3/15/2026 10:17:58 AM. This article is licensed under a Creative Commons Attribution-NonCommercial 3.0 Unported Licence.

Table 1 Composition of Ag and Pt (mol%) characterised from STEM-EDS, ICP-MS and XPS analysis

	STEM-EDS		ICP-MS		XPS		
Sample	Ag (mol%)	Pt (mol%)	Ag (mol%)	Pt (mol%)	Ag^0 (mol%)	Pt^0 (mol%)	Pt^{2+} (mol%)
Ag NPr	100	—	100	—	100	—	—
$Ag_{98.5}Pt_{1.5}$	98.9 ± 5.0	1.1 ± 0.1	98.5 ± 0.7	1.46 ± 0.07	97.6	2.25	0.10
$Ag_{98}Pt_2$	98.8 ± 5.1	1.2 ± 0.2	97.9 ± 0.3	2.07 ± 0.30	95.5	3.85	0.67
$Ag_{96.5}Pt_{3.5}$	97.4 ± 4.9	2.6 ± 0.2	96.4 ± 1.3	3.59 ± 0.12	94.2	4.89	0.93
$Ag_{91}Pt_9$	92.6 ± 4.2	7.4 ± 0.4	92.2 ± 0.5	7.81 ± 0.46	87.2	7.04	5.73

High resolution TEM (HR-TEM) for single particle measurement do not give us conclusive indication of the existing changes as the lattice parameters of Ag and Pt are within the range of ∼5% error (Fig. S.4, ESI†). The atom-to-atom distance varied from 0.22 to 0.32 nm. These variations resulted in an average of 0.27 nm which are significantly higher than a 5% error (Fig. S.5, ESI†).

XPS analysis was conducted to investigate the efficiency of Pt deposition by GRR and determine the surface composition of the Ag Pt NPs (Fig. 3). Ag 3d spectra of Ag NPr showed binding energy peaks at 367.7 eV ($3d_{5/2}$ spin–orbit component), corresponding to Ag^0 [49] (Fig. 3A). The Ag $3d_{5/2}$ peaks in AgPt NPrs also showed similar peak profiles at ∼367.7 eV, while no signals were observed for Ag^+. For AgPt, Pt 4f spectra showed both Pt^0 and Pt^{2+} signals with binding energies at 70.1 and 72 eV of $4f_{7/2}$ spin orbital[50,51] (Fig. 3B). The intensity of the Pt^{2+} signal was proportional to Pt loading, thus showing the limited extent of GRR. The XPS results were used to quantify the elemental composition of Ag^0, Pt^0 and Pt^{2+} in the different samples (Table 1). C 1s spectra for Ag NPr showed peaks at 285 eV (C–H), 286.5 eV (C–O) and 288 eV (C═O), which likely results from the citrate used as capping agent.[52] Similarly, O 1s spectra for Ag NPr showed peaks at ∼531 eV (C═O) and 533 eV (C–O/C–OH) (Fig. S.6, ESI†).[53] The peak signals corresponding to C═O were significantly lower on $Ag_{91}Pt_9$, resulting from the loss of capping agent on the surface.[49]

Table 1 summarises the metal composition measured through various techniques. The measurements from STEM-EDS of particle maps and ICP-MS of bulk solution were in good agreement and were close to theoretical estimates. Results from XPS quantification corresponded to the surface composition, which showed higher Pt loading. This was expected as XPS is a surface-sensitive technique. This is in agreement with the surface-limited bimetallic structure seen in STEM line scans (Fig. S.3, ESI†). Of the total Pt signals, Pt^{2+} increased from ∼4.3% to ∼45% with increasing Pt loading. This indicated that the degree of galvanic reduction was inversely correlated with the Pt loading.

Photocatalytic CO_2 hydrogenation

Effect of Pt loading. We investigated the addition of Pt towards the product selectivity in aqueous-phase CO_2 hydrogenation operated in a batch photo reactor (Fig. S.7A and B, ESI†) at 10 bar. The catalyst loading was selected based on wavelength absorbance to reduce optical saturation (Fig S.7D and Table S.3, ESI†). HCOOH, HCHO and CH_3COOH were detected as liquid products, whereas no gaseous products were obtained. As seen in Fig. 4A, adding 1.5 mol% Pt significantly improved the HCOOH yield by approximately 10-fold, to 0.42 ± 0.12 mmol g_{cat}^{-1}. A maximum HCOOH yield of 0.52 ± 0.08 mmol g_{cat}^{-1} was obtained at 2 mol% Pt. Similarly, the highest HCHO yield of 0.16 ± 0.01 mmol g_{cat}^{-1} was obtained at 3.5 mol% Pt. With 9 mol% Pt loading, we observed the highest CH_3COOH yield of 0.43 ± 0.03 mmol g_{cat}^{-1}. This trend revealed that the yield of products requiring higher electron consumption increased with the Pt loading. To validate that this reaction was not driven by Pt solely, we performed the reaction with Pt NPs, which yielded comparably low amounts of HCOOH and CH_3COOH.

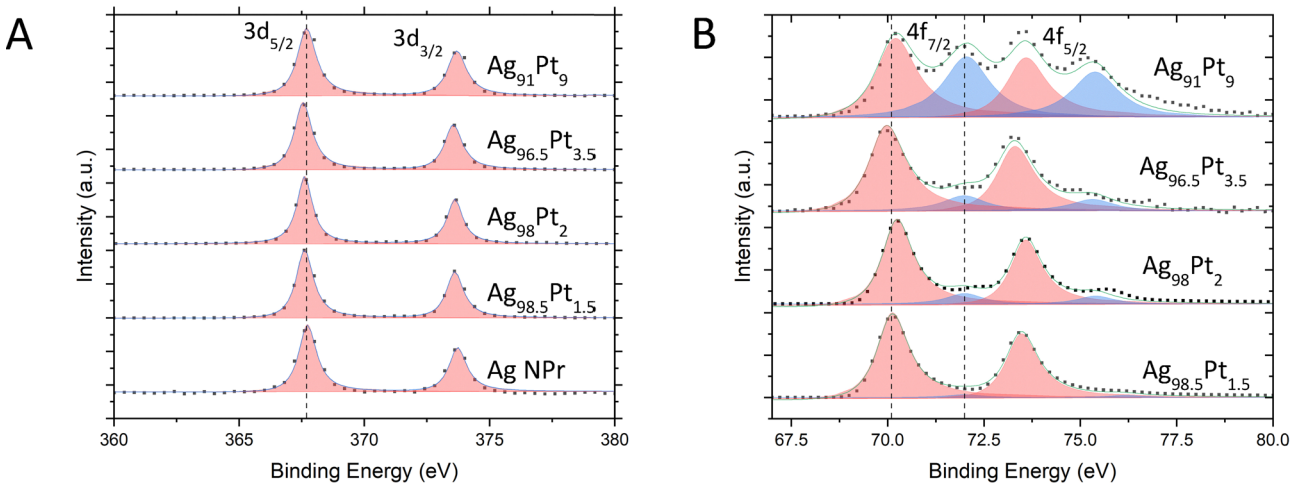

Fig. 3 XPS spectra of AgPt NPrs in (A) Ag 3d region and (B) Pt 4f region.

 © 2025 The Author(s). Published by the Royal Society of Chemistry

Open Access Article. Published on 22 April 2025. Downloaded on 3/15/2026 10:17:58 AM.
This article is licensed under a Creative Commons Attribution-NonCommercial 3.0 Unported Licence.

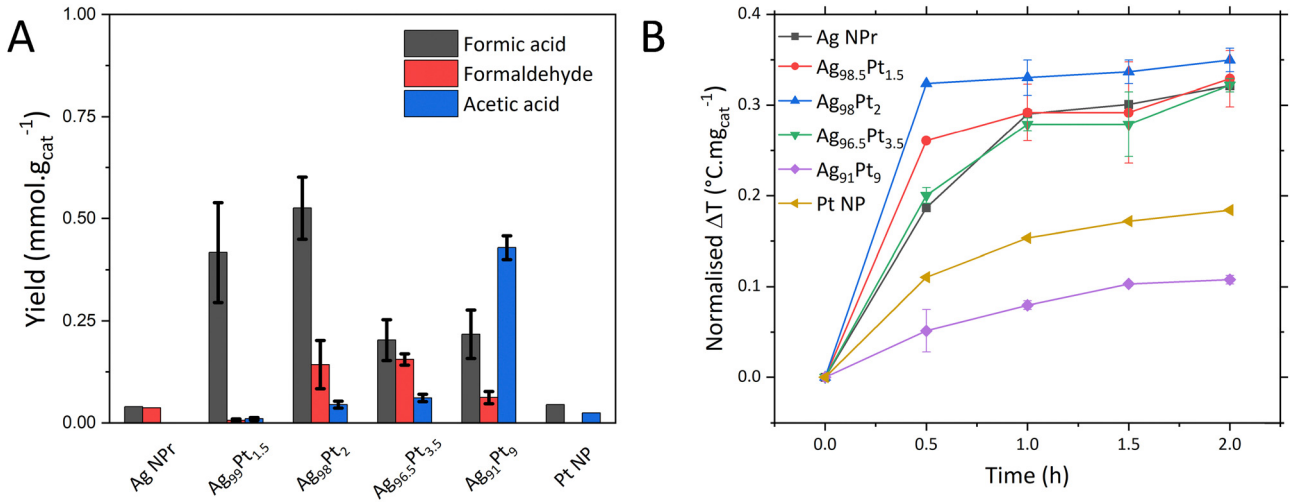

Fig. 4 (A) Product yield of AgPt surface alloyed catalysts with different Pt loadings (B) *in situ* temperature profile of the reactor solution. Reaction conditions – pressure = 10 bar (H_2/CO_2 = 1), filtered Xe lamp illumination, t = 2 h.

In situ temperature profile was measured during the reaction to investigate the effect of Pt loading on the plasmon decay pathway (Fig. 4B). The trend of photothermal response indicated that low Pt loading did not significantly affect the photothermal response, suggesting that electron relaxation to thermalisation was not affected. The highest *in situ* temperature of ~0.35 °C/mg$_{cat}$ was observed in $Ag_{98}Pt_2$ whereas $Ag_{91}Pt_9$ showed a relatively lower rate and steady-state temperature. The correlation between dampened extinction intensity of the plasmon resonance peaks and temperature increase was similarly reported for Au/Pd system.[54] The plasmon decay for Ag–Pt system has been reported to under electron and energy transfer, therefore reducing heat generation.[41,55]

A series of control reactions verified the visible-light photocatalytic activity of AgPt NPrs. Catalysts were irradiated with a 300 W Xe Lamp in unfiltered and filtered modes corresponding to different spectral intensity profiles (Fig. S.7C, ESI†). As seen in Fig. 5, the product selectivity between the illumination modes varied at lower Pt loadings. This difference in the selectivity at lower Pt loading was due to electrons generated by the interband transitions in Ag that lied in the UV region (Fig. 1 and 5A, B). As the Pt loading increased, the product selectivity was relatively similar as the plasmon decay pathway dissipated towards surface AgPt sites, thus governing the catalytic pathway (Fig. 5C and D).[38] A control reaction with no illumination (reaction in dark) was also conducted for $Ag_{91}Pt_9$, which produced 0.11 mmol g_{cat}^{-1} HCOOH and <0.01 mmol g_{cat}^{-1} HCHO. The aqueous production of HCOOH has a negative Gibbs free energy and is favourable at these conditions.[56] The apparent quantum yield (AQY) was calculated for the cumulative production of HCOOH, HCHO and CH_3COOH against the photons emitted in the two illumination modes. The increase in AQY in the filtered mode increased proportional to the Pt loading, thus confirming the visible-light driven nature of the $Ag_{100-x}Pt_x$ nanoprisms.

Further control reactions were conducted using $Ag_{91}Pt_9$ to validate the consumption of CO_2 and H_2 (Fig. S.13, ESI†). The reaction did not proceed without any catalyst. A 100% CO_2 environment yielded 0.012 mmol g_{cat}^{-1} HCOOH and 0.053 mmol g_{cat}^{-1} HCHO. While Ag-based catalysts have shown HCOOH and HCHO production in similar applications using H_2O as the electron-donating species, this reaction relied on the presence of H_2 as the electron donor.[57–59] To confirm the absence of any other carbon sources in the reaction, a 100% H_2 environment was used. We observed the formation of HCOOH at 0.11 mmol g_{cat}^{-1}, HCHO at 0.026 mmol g_{cat}^{-1} and CH_3COOH at 0.01 mmol g_{cat}^{-1}. This contradicted our initial assumption. However, we detected ~280 μM bicarbonate (HCO_3^-) from HPLC analysis in the solution before the reaction commenced which decreased to 190 μM, indicating that CO_2 from the air was absorbed and converted into aqueous species, such as HCO_3^- and carbonate (CO_3^{2-}), in the feed solution.

To validate the source of carbon species responsible for forming the C_1 and C_2 products in this study, the feed solution was dosed with 0.5 mM HCO_3^- and H_2. The results showed increased product yields, with the maximum yields of HCOOH, HCHO and CH_3COOH at 0.19 mmol g_{cat}^{-1}, 0.072 mmol g_{cat}^{-1}, and 0.125 mmol g_{cat}^{-1}, respectively. This confirmed that HCO_3^- was a precursor to the hydrogenation reaction in a similar yield trend to that of H_2 + CO_2 environment. Photo-oxidation of adsorbed citrate capping on Ag NPr to CO_2 has been observed.[60] Hence, we dosed a reaction containing 0.5 mM sodium tricitrate and H_2. No products were detected until 1 h, similar to the 100% H_2 environment case, which showed negligible contribution from citrate.

The optical properties of the NPrs were analysed *ex situ* at different reaction times (Fig. S.8, ESI†). The plasmon resonance peaks observed in Ag NPr did not change. However, a blue shift was observed in the AgPt NPrs. This suggested changes in the adsorbed surface species on the NPrs, although further investigations were conducted to determine possible causes.[58,61] XPS analysis of the NPrs post-reaction showed some BE shifts for Ag 3d and Pt 4f regions compared to as-synthesised NPrs (Fig. S.9, ESI†). The Ag $3d_{5/2}$ peak for Ag NPr shifted the most from 367.7 eV to 368 eV. The BE shift was reduced with increasing Pt

Open Access Article. Published on 22 April 2025. Downloaded on 3/15/2026 10:17:58 AM.
This article is licensed under a Creative Commons Attribution-NonCommercial 3.0 Unported Licence.

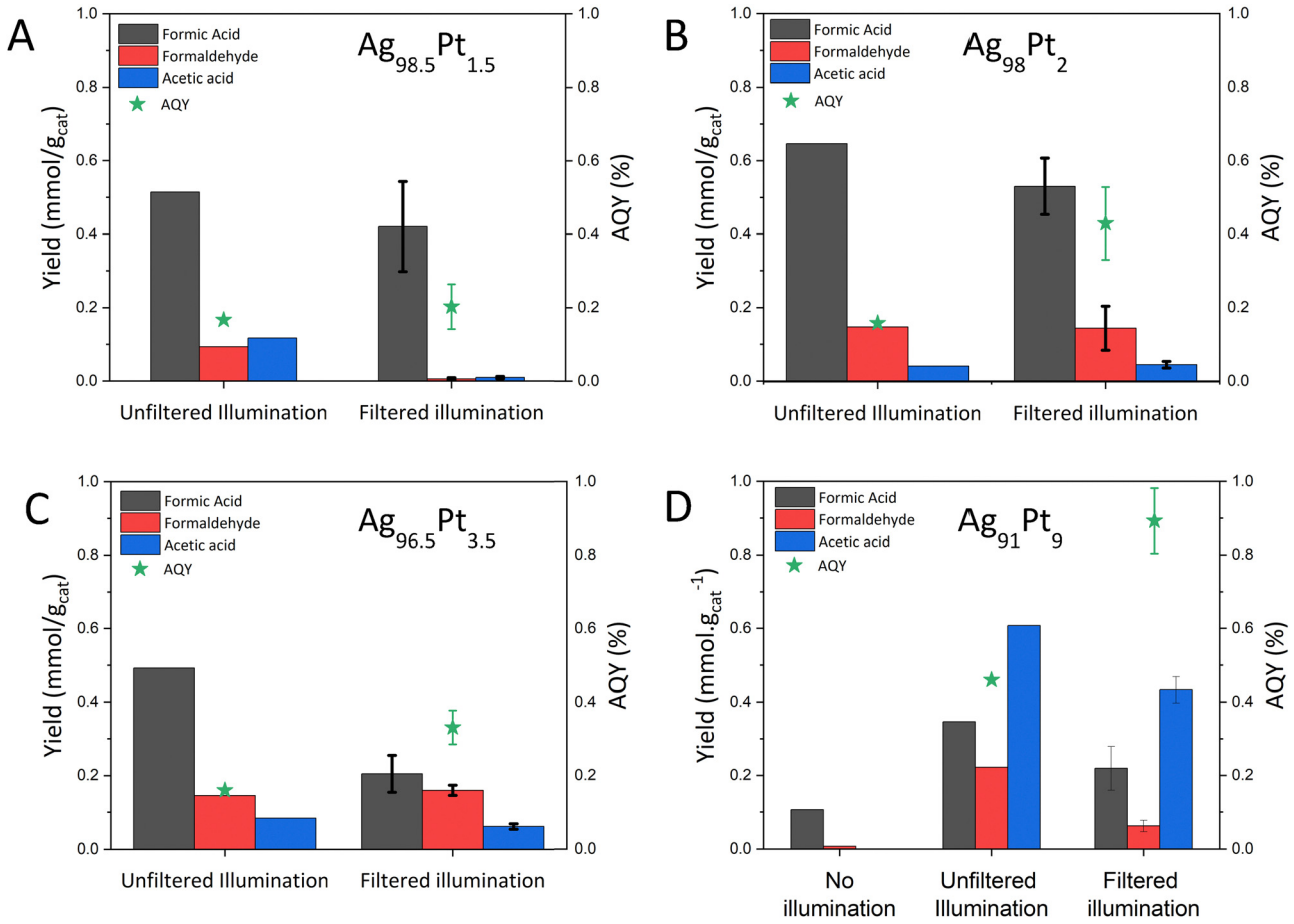

Fig. 5 Product yields and AQY under unfiltered Xe lamp illumination (320–2500 nm) and Filtered Xe lamp illumination (380–780 nm) of (A) $Ag_{98.5}Pt_{1.5}$ (B) $Ag_{98}Pt_2$ (C) $Ag_{95.5}Pt_{3.5}$ (D) $Ag_{91}Pt_9$ reaction conditions – ~10 mg catalyst, P = 10 bar, H_2/CO_2 (1 : 1 v/v), t = 2 h.

loading. Similarly, the highest BE shift in Pt $4f_{7/2}$ was observed for $Ag_{98.5}Pt_{1.5}$ from 70.1 eV to 70.5 eV. We deduce these shifts in binding energy indicate diffusion of Ag to form an Ag–Pt surface alloy adlayer.[62]

Aggregation of NPrs was observed among all samples under reaction conditions (Fig. S.10A, ESI†), which was hypothesised to be because of either the loss of capping agent or structural changes. Upon the introduction of reaction gases, a decrease in pH occurred due to. the solvation of CO_2, which created an acidic medium. The decrease in pH increases the protonation of trisodium citrate, which could cause NPrs aggregation.[63] Analysis of the solutions pre- and post-reaction revealed an average pH reduction from 6.9 to 4.9 (Fig. S.10B, ESI†). The shift in pH would cause protonation of $[Citrate]^{3-}$ to $H_2[Citrate]^-$ and affect the surface charge of the NPr. Therefore, we investigated the change in surface charge by measuring the zeta potential and hydrodynamic radius of the NPrs post-reaction (Fig. S.10C, ESI†). The zeta potential of as-synthesised AgPt NPrs averaged at −28 mV with a mean hydrodynamic radius of 48 nm. The zeta potential of the NPrs post-reaction increased compared to the initial measurement, where this increase was proportional to the Pt loading. Similarly, the hydrodynamic radius increased proportionally to the Pt loading with a mean hydrodynamic radius of ~80 nm for $Ag_{91}Pt_9$. XPS analysis of post-reaction AgPt NPrs in C 1s region (Fig. S.9C, ESI†) also showed a significant decrease in the signal area for C═O (288 eV), confirming the cause of aggregation from loss of citrate from the particle surface. This implied that the acidic environment formation of acidic products further caused citrate protonation and particle aggregation.[64]

On the nanoscale, examples of NPrs with structural deformations, such as holes on particle faces, were seen in pre- and post-reaction samples. The frequency of hole formation was higher in the post-reaction samples (Table S.4 and Fig. S.11, ESI†). Catalyst composition was also quantified post-reaction (Table S.5, ESI†). The composition changed compared to as-synthesised samples. However, there were discrepancies among the measurements. We considered these discrepancies as part of sample preparation techniques and analysed the data separately. In comparison, a relative increase in Pt loading of samples post-reaction was observed from ICP-MS and XPS. The increase in Pt loading implied a loss of Ag, which was not detected as Ag^+ in XPS measurements. The total catalyst recovered was also calculated using ICP-MS which showed significant Ag loss of up to 81.7% while only 10.8% Pt loss occurred in the same sample (Table S.6, ESI†). Hence, we proposed this as an unrecoverable catalyst lost during the reaction by aggregation and colloidal instability.

 © 2025 The Author(s). Published by the Royal Society of Chemistry

Open Access Article. Published on 22 April 2025. Downloaded on 3/15/2026 10:17:58 AM.
This article is licensed under a Creative Commons Attribution-NonCommercial 3.0 Unported Licence.

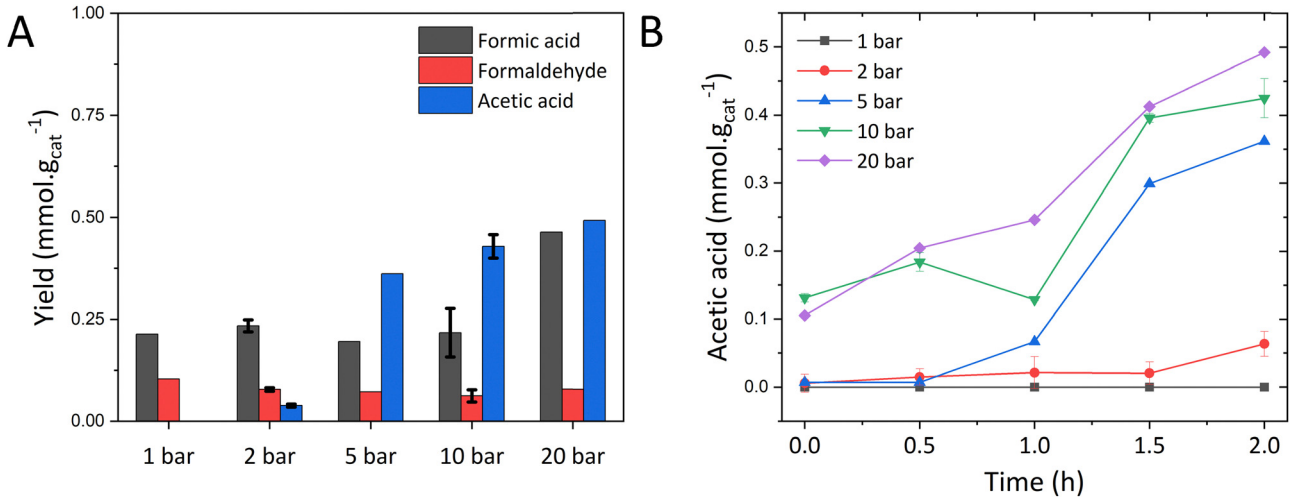

Fig. 6 (A) Product yield of $Ag_{91}Pt_9$ as a function of pressure (B) CH_3COOH yield profile at different pressures. Reaction conditions – ~10 mg catalyst, H_2/CO_2 (1 : 1), room temperature, filtered illumination mode.

Measurements from STEM-EDS indicated no significant compositional change occurred to the imaged NPrs (Table S.5, ESI†).

Impact of reaction pressure. The effect of pressure on the product yields was investigated because of the low solubility of H_2 at ambient pressures (Fig. 6A). With increasing pressure, HCOOH production was favoured with the maximum yield of 0.46 mmol g_{cat}^{-1} at 20 bar. This confirmed the pressure dependence of the photocatalytic reactions and was likely produced by the hydrogenation of dissolved CO_2.[65] The HCHO yield was not affected significantly by increasing pressure. CH_3COOH was not observed at 1 bar, followed by a significant increase to 0.36 mmol g_{cat}^{-1} at 5 bar and reached a maximum yield of 0.49 mmol g_{cat}^{-1} at 20 bar. The yield profile of CH_3COOH over the reaction time showed a trend where the production of CH_3COOH production was only observed after 1 h at 5 bar, but reached a near-linear productivity of ~0.196 mmol g_{cat}^{-1} h^{-1} at 20 bar (Fig. 6B). We deduced that the hydrogenation of CO_2 was limited by mass transfer below 5 bar. This was overcome at higher pressures but reached a kinetic limitation of the rate-determining step, as observed by the incremental change in CH_3COOH yield between 5–20 bar (Fig. S.12A, ESI†). We also investigated the colloidal stability as a function of pressure. The pH of the solution decreased at higher reaction pressures owing to the increased solubility of CO_2. As a result, the zeta potential and hydrodynamic radius increased to −0.25 mV and 144 nm respectively, implying increased extent of aggregation (Fig. S.12B and C, ESI†).

Distinguishing plasmon-mediated catalysis. Because of the anisotropic shape of Ag NPr, multiple LSPR peaks were observed corresponding to in-plane and out-of-plane dipole and quadrupole plasmon resonances (Fig. 1). To distinguish the effect of LSPR peak on catalyst performance, the impact of illumination wavelength was investigated on the product yield of CO_2 hydrogenation using $Ag_{91}Pt_9$ (Fig. 7). Using a supercontinuum laser with a contrast filter, the excitation wavelengths between 400–900 nm could be controlled to a bandwidth of less than 2.5 nm. Product yields were normalised using the irradiation power (mW). The highest yield contribution of 0.57 mmol g_{cat}^{-1} mW^{-1}, was revealed by trends in HCOOH yield at the in-plane dipole

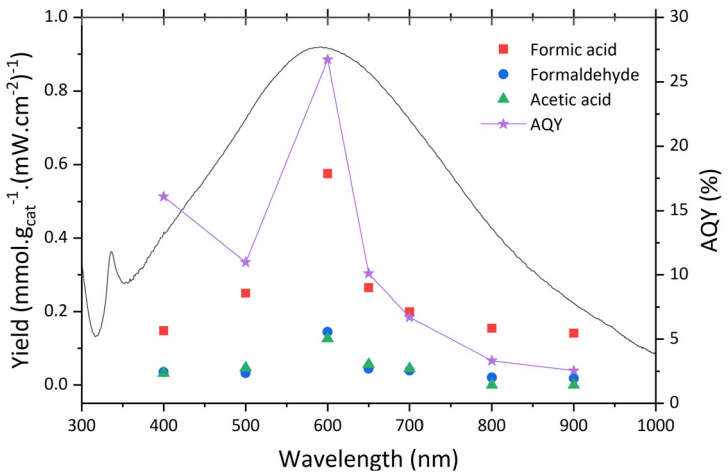

Fig. 7 Wavelength-dependent product yields normalised by laser power. Black line shows extinction spectra for $Ag_{91}Pt_9$ post-reaction.

Open Access Article. Published on 22 April 2025. Downloaded on 3/15/2026 10:17:58 AM.
This article is licensed under a Creative Commons Attribution-NonCommercial 3.0 Unported Licence.

resonance peak (600 nm) of $Ag_{91}Pt_9$. This also coincided with the highest AQY of 26.7%. CH_3COOH was not detected at wavelengths higher than 700 nm. At 600 nm, the highest *in situ* temperature of 1.7 °C was observed (Fig. S.14A, ESI†). The peak temperature profile correlated well with the yield profile, confirming that plasmon generation was the highest at the in-plane dipole and significantly increased the catalytic performance. HCHO and CH_3COOH exhibited higher selectivity at lower wavelengths (400–500 nm), possibly because of the energy of hot carriers, which is proportional to the energy of the illuminating photon (Fig. S.14B, ESI†). Interestingly, we observed that the yield of HCHO and CH_3COOH were in the same magnitudes across all wavelengths except >700 nm where no CH_3COOH was produced. This implied a rate-limiting step that affected the C–C coupling to CH_3COOH.

Reaction pathway investigation. Based on a study conducted by Genovese and co-authors,[66] the reaction pathway to CH_3COOH was investigated by using several intermediates ($NaHCO_3$, HCOOH, HCHO, CH_3OH) observed during CO_2 hydrogenation (Table S.7, ESI†). Using $NaHCO_3$ produces HCO_3^- as a reactant that produced all liquid products. Based on previous literature findings, HCO_3^- approaches equilibrium with aqueous CO_2 and create COO^- on the catalyst surface that was a key reaction intermediate. Comparatively, using HCOOH and HCHO did not yield CH_3COOH significantly higher than control reaction 2 (Fig. S.13, ESI†). This implied that *HCOO and *CHO were not the intermediates involved in C–C coupling towards CH_3COOH. This also suggested that adsorption of these radicals inhibited CH_3COOH production, as the oxidation of these intermediates was not favourable. Using CH_3OH, however, produced a relatively higher CH_3COOH yield, implying $*CH_3$ as a key intermediate for the reaction. Contrarily, the oxidation of CH_3OH as a hole scavenger could also produce CO_2, contributing to the reaction pathway.[67] Therefore, we conducted a control reaction involving $NaHCO_3$ and CH_3OH that produced a higher yield of CH_3COOH. From these reactions, we deduce that CO_2/COO^- and $*CH_3$ were key reaction intermediates in the C–C coupling to CH_3COOH and *HCOO/*CHO resulted from CO_2 hydrogenation but did not participate directly in C–C coupling.

Based on the liquid products observed, the reaction pathway was elucidated based on similar findings from previous studies.[66,68] As shown in Scheme 1, the reaction initiates with the adsorption of CO_2 resulting from dissolved CO_2 and HCO_3^-. The formation of HCOOH was followed by a two-step electron reduction involving COO^- and $*HCOO^-$. HCHO was produced by further hydrogenating $*HCOO^-$ to *CHO and $*CH_2O$. $*CH_3$ was produced from $*CH_2O$, undergoing a nucleophilic reaction from COO^- to produce CH_3COO^-/CH_3COOH.

Discussion

The CO_2 hydrogenation performance of $Ag_{91}Pt_9$ NPrs was comparable with other metal-based photocatalysts reported in the literature (Table S.8, ESI†). While HCOOH and HCHO were

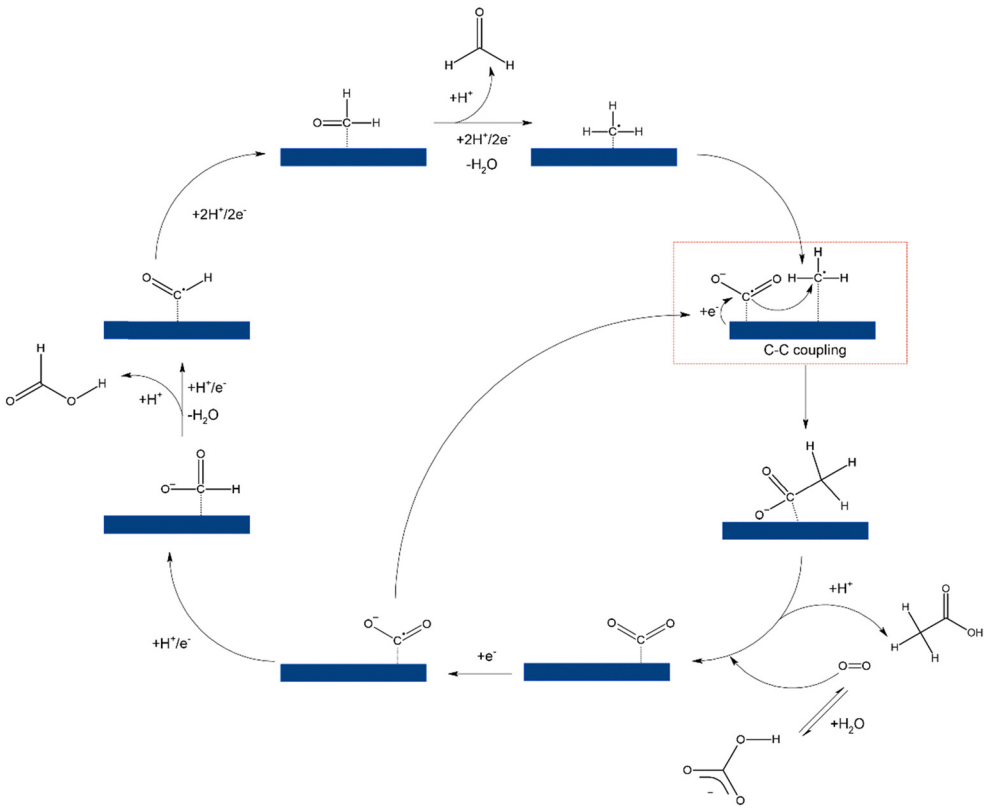

Scheme 1 Proposed reaction pathway of CO_2 to HCOOH, HCHO and CH_3COOH on AgPt NPr.

 © 2025 The Author(s). Published by the Royal Society of Chemistry

Open Access Article. Published on 22 April 2025. Downloaded on 3/15/2026 10:17:58 AM.
This article is licensed under a Creative Commons Attribution-NonCommercial 3.0 Unported Licence.

produced in similar yields, CH_3COOH was produced at a much higher yield. This could be attributed to the favourability of C–C coupling on AgPt NPrs and optimal reaction conditions. Although most reaction conditions involved H_2O as the electron donor to reduce CO_2 to CO, using H_2 in our experiments significantly improved the product yields. H_2 is used in CO_2-to-CH_3OH, which favours $*CH_3$ formation. Using a liquid-phase reaction also favoured certain products, and the reaction pressure improved the mass transfer of reactants in the solution. This study conducted the reactions at room temperature and confirmed the catalyst was primarily active in the visible light region. Therefore, the reaction was considered to be plasmon-mediated and driven by visible-light illumination. We observed correlations between the LSPR peaks and *in situ* temperature; however, this did not confirm the exact mechanism of plasmon decay. With the addition of Pt, the plasmon decay mechanism shifted towards energy transfer and hot-electron generation. Further investigation would provide insight into this mechanism. Increasing Pt loading and reaction pressure affected the colloidal stability. The aggregation presented a limitation on the parameters that could be investigated. An alternative capping agent such as polyvinylpyrrolidone (PVP) and cetyltrimethylammonium bromide (CTAB) could improve the colloidal stability. In order to create a scalable synthesis, catalyst immobilisation on a support or encapsulation in microparticle frameworks could help overcome this limitation. Further improvement in achieving high AQY could be approached by designing a modular reactor system which ideal wavelength illumination in a continuous mode.

Conclusions

We have developed a bimetallic plasmon-active catalyst consisting of a combination of the Ag–Pt system for photocatalysis. The incorporation of Pt into Ag NPrs as surface-limited alloys significantly improved the product yield and selectivity by altering the plasmon decay pathway towards energy transfer from Ag to Pt. The maximum yields of HCOOH (0.52 mmol g_{cat}^{-1} with $Ag_{98}Pt_2$), HCHO (0.16 mmol g_{cat}^{-1} with $Ag_{96.5}Pt_{3.5}$ and CH_3COOH (0.43 mmol g_{cat}^{-1} with $Ag_{91}Pt_9$) suggested multi-electron hydrogenation and C–C coupling of $*CH_3$ and COO^- species. Notably, a peak AQY of 26.7% was observed at the in-dipole resonance (600 nm) for $Ag_{91}Pt_9$, highlighting the wavelength dependence in driving the reaction. Catalyst deactivation due to colloidal instability and long-term performance validation remains a challenge. Therefore, future work on improving catalyst stability and investigating surface species will provide deeper insight on the viability for scale-up. These findings highlight the role of designer plasmonic catalysts in enhancing photocatalytic CO_2 conversion. The results demonstrate that careful tuning of catalyst composition and morphology significantly improve the light-to-energy transfer and product selectivity.

Experimental

Chemicals

Silver nitrate ($AgNO_3$), trisodium citrate dihydrate, sodium borohydride ($NaBH_4$), poly(4-styrenesulfonic acid)sodium salt (PSSS, 1000 kDa), L-ascorbic acid, potassium tetrachloroplatinate(II) (K_2PtCl_4), formic acid (reagent grade), acetic acid (reagent grade) and methanol (ACS reagent) were purchased from Sigma Aldrich and used as received. CO_2 (ultra-high purity) and H_2 (ultra-high purity) was purchased from BOC. MilliQ water (18.2 mΩ) was used for all the experiments.

Synthesis of Ag NPr and $Ag_{100-x}Pt_x$ nanoparticles

Ag seed synthesis. 5 mL of 2.5 mM trisodium citrate, 0.3 mL of 10 mM $NaBH_4$ and 0.25 mL of 500 mg L^{-1} PSSS were stirred until mixed under ambient conditions. 5 mL $AgNO_3$ was added at a rate of 2 mL minute^{-1} under stirring. The Ag seed solution was aged at room temperature without protection from light for 4–6 hours.

Ag NPr synthesis. 75 μL of 10 mM ascorbic acid, 5 mL Milli-Q H_2O and 47 μL Ag seed solution were mixed under ambient conditions. Under stirring, 3 mL $AgNO_3$ was added at a rate of 1 mL minute^{-1}. After 2 additional minutes of stirring, 5 mL of 25 mM trisodium citrate was added. The sample was mixed for another 2 minutes before the synthesis was complete.

$Ag_{100-x}Pt_x$ synthesis. A chosen volume of Ag NPr solution was stirred in dark. The molar mass of Ag present in this solution was calculated based upon the synthesis process. The appropriate mass of Pt precursor for the desired Pt loading was then calculated (*e.g.* for 500 mL of $Ag_{91}Pt_9$, 3.64 mg K_2PtCl_4 was needed). The Pt precursor was dissolved in a small volume of Milli-Q H_2O before being added to the stirring Ag NPr solution. The volume of H_2O used was arbitrarily set to 5 mL but did not affect the synthesis.

Characterisations

UV-vis extinction spectra of the samples were obtained using a PerkinElmer Lambda 365 UV-vis spectrophotomer. Samples to be imaged in STEM were centrifuged three times at 10k RPM for 30 minutes. The supernatant was removed and replaced with Milli-Q H_2O. 1.4 μL of sample solution was drop cast on plasma-cleaned carbon-film-coated Cu grids. STEM imaging was captured on both the FEI Tecnai G2 T-20 TWIN TEM and F20 S-TWIN TEM at Monash Centre for Electron Microscopy (MCEM). STEM-EDS was conducted on the F20 using a Bruker 30 mm^2 123 eV windowless SDD and Quantax analysis system. ^{107}Ag and ^{195}Pt isotope concentrations were analysed in the bulk catalyst samples using Inductively Coupled Plasma – Mass Spectroscopy (Thermo iCAP TQe Triple Quadrupole). 2 mL of catalyst samples were diluted in 70% v/v HNO_3 followed by serial dilutions in 2% v/v HNO_3. Sample zeta potentials and hydrodynamic radius were measured and recorded by Malvern Nano Zetasizer using disposable folded capillary cells (DTS1070). XPS analysis of as-synthesised nanoparticles was conducted on Thermo Scientific K-alpha XPS (monochromated Al Kα, E_{photon} = 1487.6 eV, 1×10^{-9} torr). Scans were obtained using a pass energy of 50 eV with 0.1 eV resolution. Post-reaction samples were analysed on the Thermo Nesa Surface Analysis System (monochromated Al Kα, E_{photon} = 1487.6 eV). The spectra were charge corrected to adventitious carbon at 285 eV in the C 1s region using Avantage software. Ag 3d and P 4f regions were background corrected with Shirley algorithm. Ag^0 and Pt^0

Open Access Article. Published on 22 April 2025. Downloaded on 3/15/2026 10:17:58 AM. This article is licensed under a Creative Commons Attribution-NonCommercial 3.0 Unported Licence.

peaks were fitted with a Doniac-Sunjic asymmetry model. The oxidation states (Pt^{2+}), C 1s and O 1s regions were equipped with Gaussian–Lorentzian function in Origin software (2022b).

Photocatalytic CO_2 hydrogenation

The reaction was carried out in batch mode in a PARR (A239M) photoreactor with a K-type thermocouple inserted at the base. 5–10 mg of as-synthesised catalysts were concentrated, re-dispersed in 50 mL Milli-Q H_2O and added to the reaction vessel. The reactor was sealed, and H_2 was introduced for 15 min to flush the reactor. This was followed by venting the reactor and introducing CO_2 and H_2 (1 : 1) to the specified pressure. A 300 W Xe lamp (Zolix 300P) irradiated the sample through the photoreactor window. For visible light (380–780 nm) irradiation, a UV + IR cutoff filter was used. Liquid products were analysed using high-performance liquid chromatography (Agilent 1220 Infinity). An ion exclusion column (Rezex RHM-Monosaccharide H+ 8%) with refractive index detector was used to detect HCOOH and CH_3COOH). A C18 column (Xterra MS C18) with diode array detector was used to detect HCHO by derivatisation with Nash reagent. Gaseous products (CO, CO_2, CH_4 and H_2) were analysed using gas chromatography (Agilent MicroGC 990) equipped with a TCD detector. Wavelength-dependent studies were performed using the same photoreactor setup as NKT Supercontinuum source (SuperK Fianium FIU-15) with a LTTF Contrast VIS giving a bandwidth <2.5 nm.

Equations

$$\text{Yield}\left(\text{mmol } g_{\text{cat}}^{-1}\right) = \frac{C_{\text{product}}\ (\text{mM}) \times V_{\text{reactor}}\ (\text{L})}{m_{\text{cat}}\ (\text{g})}$$

$$\text{Selectivity}\ (\%) = \frac{n_{\text{product}}\ (\text{mol})}{n_{\text{total}}\ (\text{mol})} \times 100$$

$$\text{AQY}\ (\%) = \frac{\text{number of reacted electrons}}{\text{number of incident photons}} \times 100$$

where,

$N_{\text{formic acid}} = 2$

$N_{\text{formaldehyde}} = 4$

$N_{\text{acetic acid}} = 8$

Data availability

All data has been included in the manuscript and ESI.† Raw data may be provided upon request.

Conflicts of interest

There are no conflicts to declare.

Acknowledgements

This research is supported by the Australian Research Council (ARC) Research Hub for Carbon Utilisation & Recycling (RECARB Hub) (IH220100012), Monash University, BASF Australia Ltd and Woodside Energy Technologies Pty Ltd. The authors would like to thank Woodside Monash Energy Partnership for financial support. The authors acknowledge the use of the instruments and scientific and technical assistance at the Monash Centre for Electron Microscopy, a node of Microscopy Australia. This research used equipment funded by the Australian Research Council grant LE110100223. The authors acknowledge the use of facilities within the Monash X-ray Platform. The authors acknowledge the facilities, and the scientific and technical assistance of the RMIT University's Microscopy & Microanalysis Facility, a linked laboratory of Microscopy Australia, enabled by NCRIS The authors acknowledge the assistance of Prof. Terence Turney and thank him for his advice and feedback. Prof. Stefan A. Maier acknowledges the Lee-Lucas Chair in Physics.

Notes and references

1 G. Garcia-Garcia, M. C. Fernandez, K. Armstrong, S. Woolass and P. Styring, *ChemSusChem*, 2021, **14**, 995–1015.
2 W. Ahmad, G. Bhardwaj, R. Lakshman, P. Koley and A. Tanksale, *Energy Fuels*, 2023, **37**, 19377–19399.
3 Y. Wang, E. Chen and J. Tang, *ACS Catal.*, 2022, **12**, 7300–7316.
4 M. Tahir and N. A. S. Amin, *Int. J. Hydrogen Energy*, 2017, **42**, 15507–15522.
5 J. Zhao, B. Liu, L. Meng, S. He, R. Yuan, Y. Hou, Z. Ding, H. Lin, Z. Zhang, X. Wang and J. Long, *Appl. Catal., B*, 2019, **256**, 117823.
6 G. Chen, R. Gao, Y. Zhao, Z. Li, G. I. N. Waterhouse, R. Shi, J. Zhao, M. Zhang, L. Shang, G. Sheng, X. Zhang, X. Wen, L.-Z. Wu, C.-H. Tung and T. Zhang, *Adv. Mater.*, 2018, **30**, 1704663.
7 S. Xue, C. Wei, M. Shen, X. Liang, J. Wang, C. Yang, W. Xing, S. Wang, W. Lin, Z. Yu, Y. Hou, J. C. Yu and X. Wang, *Proc. Natl. Acad. Sci. U. S. A.*, 2024, **121**, e2319751121.
8 D. Zeng, H. Wang, X. Zhu, H. Cao, W. Wang, Y. Zhang, J. Wang, L. Zhang and W. Wang, *Appl. Catal., B*, 2023, **323**, 122177.
9 K. Tamaki, P. Verma, T. Yoshii, T. Shimojitosho, Y. Kuwahara, K. Mori and H. Yamashita, *Catal. Today*, 2023, **411–412**, 113795.
10 R. Kuriki, K. Sekizawa, O. Ishitani and K. Maeda, *Angew. Chem., Int. Ed.*, 2015, **54**, 2406–2409.
11 L. F. Garay-Rodríguez and L. M. Torres-Martínez, *J. Mater. Sci.: Mater. Electron.*, 2020, **31**, 19248–19265.
12 W. Hou, W. H. Hung, P. Pavaskar, A. Goeppert, M. Aykol and S. B. Cronin, *ACS Catal.*, 2011, **1**, 929–936.
13 Z.-j Wang, H. Song, H. Pang, Y. Ning, T. D. Dao, Z. Wang, H. Chen, Y. Weng, Q. Fu, T. Nagao, Y. Fang and J. Ye, *Appl. Catal., B*, 2019, **250**, 10–16.
14 D. Wu, K. Deng, B. Hu, Q. Lu, G. Liu and X. Hong, *ChemCatChem*, 2019, **11**, 1598–1601.
15 M. Izadpanah Ostad, M. Niknam Shahrak and F. Galli, *J. CO2 Util.*, 2021, **43**, 101373.
16 N. Li, X. Liu, J. Zhou, W. Chen and M. Liu, *Chem. Eng. J.*, 2020, **399**, 125782.
17 Y. Meng, L. Zhang, H. Jiu, Q. Zhang, H. Zhang, W. Ren, Y. Sun and D. Li, *Mater. Sci. Semicond. Process.*, 2019, **95**, 35–41.

 © 2025 The Author(s). Published by the Royal Society of Chemistry

Open Access Article. Published on 22 April 2025. Downloaded on 3/15/2026 10:17:58 AM.
This article is licensed under a Creative Commons Attribution-NonCommercial 3.0 Unported Licence.

18 S. Unser, I. Bruzas, J. He and L. Sagle, *Sensors*, 2015, **15**, 15684–15716.
19 Z. Zhang, W. Shen, J. Xue, Y. Liu, Y. Liu, P. Yan, J. Liu and J. Tang, *Nanoscale Res. Lett.*, 2018, **13**, 54.
20 C. Clavero, *Nat. Photonics*, 2014, **8**, 95–103.
21 C. Hu, X. Chen, J. Jin, Y. Han, S. Chen, H. Ju, J. Cai, Y. Qiu, C. Gao, C. Wang, Z. Qi, R. Long, L. Song, Z. Liu and Y. Xiong, *J. Am. Chem. Soc.*, 2019, **141**, 7807–7814.
22 H. Yin, Z. Sun, K. Liu, A. A. Wibowo, J. Langley, C. Zhang, S. E. Saji, F. Kremer, D. Golberg, H. T. Nguyen, N. Cox and Z. Yin, *Nanoscale Horiz.*, 2023, **8**, 1695–1699.
23 P. Christopher, H. Xin and S. Linic, *Nat. Chem.*, 2011, **3**, 467–472.
24 I. García-García, E. C. Lovell, R. J. Wong, V. L. Barrio, J. Scott, J. F. Cambra and R. Amal, *ACS Sustainable Chem. Eng.*, 2020, **8**, 1879–1887.
25 U. Kreibig and M. Vollmer, *Optical Properties of Metal Clusters*, Springer Berlin/Heidelberg, Berlin, Heidelberg, Berlin, Heidelberg, 1995.
26 S. A. Maier, *Plasmonics: Fundamentals and Applications*, Imprint, Springer, New York, NY: Springer US, 1st edn, 2007.
27 A. Manjavacas, J. G. Liu, V. Kulkarni and P. Nordlander, *ACS Nano*, 2014, **8**, 7630–7638.
28 K. Kolwas, *Plasmonics*, 2019, **14**, 1629–1637.
29 A. G. M. da Silva, T. S. Rodrigues, J. Wang and P. H. C. Camargo, *Chem. Commun.*, 2022, **58**, 2055–2074.
30 W. Xie, K. Zhang, R. Grzeschik and S. Schlücker, *Plasmonic Catalysis*, 2021, pp. 71–108, DOI: 10.1002/9783527826971.ch3.
31 V. V. Pham, T. Q. Nguyen, H. V. Le and T. M. Cao, *Nanoscale Adv.*, 2024, **6**, 2380–2389.
32 A. G. M. da Silva, T. S. Rodrigues, J. Wang, L. K. Yamada, T. V. Alves, F. R. Ornellas, R. A. Ando and P. H. C. Camargo, *Langmuir*, 2015, **31**, 10272–10278.
33 S. Kattel, B. Yan, J. G. Chen and P. Liu, *J. Catal.*, 2016, **343**, 115–126.
34 E. S. Gutterød, A. Lazzarini, T. Fjermestad, G. Kaur, M. Manzoli, S. Bordiga, S. Svelle, K. P. Lillerud, E. Skúlason, S. Øien-Ødegaard, A. Nova and U. Olsbye, *J. Am. Chem. Soc.*, 2020, **142**, 999–1009.
35 F. L. Chan, G. Altinkaya, N. Fung and A. Tanksale, *Catal. Today*, 2018, **309**, 242–247.
36 S. Bai, Q. Shao, Y. Feng, L. Bu and X. Huang, *Small*, 2017, **13**, 1604311.
37 Z. He, Q. Qian, J. Ma, Q. Meng, H. Zhou, J. Song, Z. Liu and B. Han, *Angew. Chem., Int. Ed.*, 2016, **55**, 737–741.
38 U. Aslam, S. Chavez and S. Linic, *Nat. Nanotechnol.*, 2017, **12**, 1000–1005.
39 V. G. Rao, U. Aslam and S. Linic, *J. Am. Chem. Soc.*, 2019, **141**, 643–647.
40 D. Aherne, D. M. Ledwith, M. Gara and J. M. Kelly, *Adv. Funct. Mater.*, 2008, **18**, 2005–2016.
41 S.-C. Lin, C.-S. Hsu, S.-Y. Chiu, T.-Y. Liao and H. M. Chen, *J. Am. Chem. Soc.*, 2017, **139**, 2224–2233.
42 W. He, X. Wu, J. Liu, K. Zhang, W. Chu, L. Feng, X. Hu, W. Zhou and S. Xie, *Langmuir*, 2010, **26**, 4443–4448.
43 J. Chen, B. Wiley, J. McLellan, Y. Xiong, Z.-Y. Li and Y. Xia, *Nano Lett.*, 2005, **5**, 2058–2062.
44 L. Ma, S.-J. Ding and D.-J. Yang, *Dalton Trans.*, 2018, **47**, 16969–16976.
45 C. Tiburski and C. Langhammer, *ACS Photonics*, 2023, **10**, 253–264.
46 F. Merkoçi, J. Patarroyo, L. Russo, J. Piella, A. Genç, J. Arbiol, N. G. Bastús and V. Puntes, *Mater. Today Adv.*, 2020, **5**, 100037.
47 Y. Chen, Z. Lai, X. Zhang, Z. Fan, Q. He, C. Tan and H. Zhang, *Nat. Rev. Chem.*, 2020, **4**, 243–256.
48 Z. Cao, Q. Chen, J. Zhang, H. Li, Y. Jiang, S. Shen, G. Fu, B.-A. Lu, Z. Xie and L. Zheng, *Nat. Commun.*, 2017, **8**, 15131.
49 K. Qi, Y. Zhang, J. Li, C. Charmette, M. Ramonda, X. Cui, Y. Wang, Y. Zhang, H. Wu, W. Wang, X. Zhang and D. Voiry, *ACS Nano*, 2021, **15**, 7682–7693.
50 E. Fidiani, G. Thirunavukkarasu, Y. Li, Y.-L. Chiu and S. Du, *J. Mater. Chem. A*, 2020, **8**, 11874–11883.
51 S.-S. Chen, X.-X. Lin, A.-J. Wang, H. Huang and J.-J. Feng, *Sens. Actuators, B*, 2017, **248**, 214–222.
52 T. Shao, D. Bai, M. Qiu, Y. Li, Q. Zhang, Z. Xue, S. He, D. Zhang and X. Zhou, *J. Ind. Eng. Chem.*, 2022, **108**, 456–465.
53 M. H. Ullah, K. Il and C.-S. Ha, *Mater. Lett.*, 2006, **60**, 1496–1501.
54 J. Gargiulo, M. Herran, I. L. Violi, A. Sousa-Castillo, L. P. Martinez, S. Ezendam, M. Barella, H. Giesler, R. Grzeschik, S. Schlücker, S. A. Maier, F. D. Stefani and E. Cortés, *Nat. Commun.*, 2023, **14**, 3813.
55 J. Bi, H. Cai, B. Wang, C. Kong and S. Yang, *Chem. Commun.*, 2019, **55**, 3943–3946.
56 S. Moret, P. J. Dyson and G. Laurenczy, *Nat. Commun.*, 2014, **5**, 4017.
57 Q. Jianping, T. Juntao, S. Jie, W. Cuiwei, Q. Mengqian, H. Zhiqiao, C. Jianmeng and S. Song, *Electrochim. Acta*, 2016, **203**, 99–108.
58 G. Kumari, R. Kamarudheen, E. Zoethout and A. Baldi, *ACS Catal.*, 2021, **11**, 3478–3486.
59 D. Devasia, A. J. Wilson, J. Heo, V. Mohan and P. K. Jain, *Nat. Commun.*, 2021, **12**, 2612.
60 P. L. Redmond, X. Wu and L. Brus, *J. Phys. Chem. C*, 2007, **111**, 8942–8947.
61 G. Kumari, X. Zhang, D. Devasia, J. Heo and P. K. Jain, *ACS Nano*, 2018, **12**, 8330–8340.
62 M. T. Schaal, M. P. Hyman, M. Rangan, S. Ma, C. T. Williams, J. R. Monnier and J. W. Medlin, *Surf. Sci.*, 2009, **603**, 690–696.
63 M. Barbalinardo, G. Ori, L. Lungaro, G. Caio, A. Migliori and D. Gentili, *J. Phys. Chem. C*, 2024, **128**, 16220–16226.
64 T. C. Prathna, N. Chandrasekaran and A. Mukherjee, *Colloids Surf., A*, 2011, **390**, 216–224.
65 P. G. Jessop, F. Joó and C.-C. Tai, *Coord. Chem. Rev.*, 2004, **248**, 2425–2442.
66 C. Genovese, C. Ampelli, S. Perathoner and G. Centi, *Green Chem.*, 2017, **19**, 2406–2415.
67 C.-T. Lin, M.-H. Shiao, M.-N. Chang, N. Chu, Y.-W. Chen, Y.-H. Peng, B.-H. Liao, H. J. Huang, C.-N. Hsiao and F.-G. Tseng, *Nanoscale Res. Lett.*, 2015, **10**, 74.
68 J. Dankar, V. Rouchon, M. Rivallan, C. Pagis and M. El-Roz, *ACS Appl. Mater. Interfaces*, 2024, **16**, 42210–42220.